(Received 2 November 2023, Accepted 8 January 2024, Scheduled 19 January 2024)

Electromagnetic Characteristic Analysis and Optimization of a Novel Reverse Salient PMSM for Wide Speed Range

Ruipan Lu, Zhangqi Liu*, Xiping Liu, Jianwei Liang, Weiliang Wu, and Wenrui Wang

College of Electrical and Automation, Jiangxi University of Science and Technology, Ganzhou 341000, China

ABSTRACT: To address the issues associated with the conventional permanent magnet synchronous machine, particularly difficulties in adjusting the air-gap flux barrier and the limited range of constant power speed regulation, this paper introduces a novel approach. It combines the intensifying-flux effect with the permanent magnet synchronous machine to propose a new design known as the reverse salient permanent magnet synchronous machine (RS-PMSM) with a multilayered flux barrier. This innovation serves to enhance the working performance of the permanent magnets. The paper's structure includes an initial introduction to the RS-PMSM, outlining its structure and operational principles. Following this, an optimization approach employing NSGA-II is used to define the RS-PMSM's optimization model. The objectives of this optimization encompass torque, torque ripple, and the reverse salient pole ratio. The study then proceeds to conduct a comprehensive set of performance analyses and comparisons, involving the initial machine, optimized machine, and a conventional machine. The performance metrics considered include no-load air-gap flux density, reverse electromotive force, torque characteristics, speed range, and efficiency. Finally, the study verifies the design rationality of the RS-PMSM, highlighting its potential to address the challenges posed by traditional permanent magnet synchronous motors.

1. INTRODUCTION

Permanent magnet synchronous machines (PMSMs) have the characteristics of high efficiency, light weight, small size, and high torque density, especially in the field of electric vehicles, and the development of permanent magnet motor has become a key technology [1–5]. Nevertheless, conventional interior permanent magnet synchronous machines necessitate an increase in i_d to expand the constant power speed range of the machine. However, this leads to an augmentation in the inverter's capacity, consequently diminishing the machine's overall efficiency. Additionally, the negative d-axis current i_d, stemming the d-axis armature reaction, poses a potential risk of irreversible demagnetization of the permanent magnet [6, 7]. This restricts the application of PMSM in situations requiring a wide constant power speed range.

To achieve a wide range of speed regulation, the intensifying-flux effect is integrated into the PMSM. The present study introduces a novel machine design capable of achieving a wide range of speeds while delivering a consistent power output, named reverse salient permanent magnet synchronous machine (RSPMSM). The RS-PMSM generates positive reluctance torque through intensifying-flux effect under low speed operating conditions, improving load carrying capacity [8, 9]. At high speeds, due to the large d-axis inductance, a smaller direct axis current can weaken the main magnetic field and broaden the speed range [10–15].

Ref. [16] proposes the method of setting five layers of flux barriers at the rotor to reduce the q axis inductance and achieve the reverse salient characteristic, which has a wider range of constant power regulation. In [17], a reverse-salient permanent magnet brushless machine with two-layer segmented permanent magnets is proposed, and the reverse-salient machine is verified to have wide speed regulation by experiment. An RS-PMSM with a special rotor structure is proposed in [18], where an arc-shaped magnetic barrier is placed on the q-axis, and the permanent magnets and magnetic bridge are arranged in an alternating V-shape. A fractional slot centralized winding with a variable saliency pole ratio is used to enable a constant power speed range of $5.5:1$. Ref. [19] proposes variable flux memory machines with low coercivity permanent magnets, which can be operated in a wider speed range by properly applying a short d-axis current pulse, enabling the adjustment of the permanent magnet flux linkage. Ref. [20] proposes an improved flux-intensifying permanent magnet machine to improve the flux weakening capability and speed range. Considering variable speed applications, the reverse saliency is optimized for constant-torque and constant power operation conditions. An optimized design of the motor using NSGA-II is presented in [21].

This paper proposes a new structure for a reverse salient permanent magnet synchronous motor (RS-PMSM) by incorporating the intensifying-flux effect. The main research objectives of this paper are as follows: In the first part, the working principle of RS-PMSM is clarified, and the basic principle of magnetic field enhancement effect is introduced. The second part involves conducting multi-objective optimization of the initial design scheme of RS-PMSM. It clarifies the optimization process, objective function, and design variables. The design variables are analyzed for sensitivity and stratified, and the NSGA-II algorithm is employed to obtain the topology with optimal performance. In the third part, the electromagnetic perfor-

* Corresponding author: Zhangqi Liu (liuzhq@jxust.edu.cn).

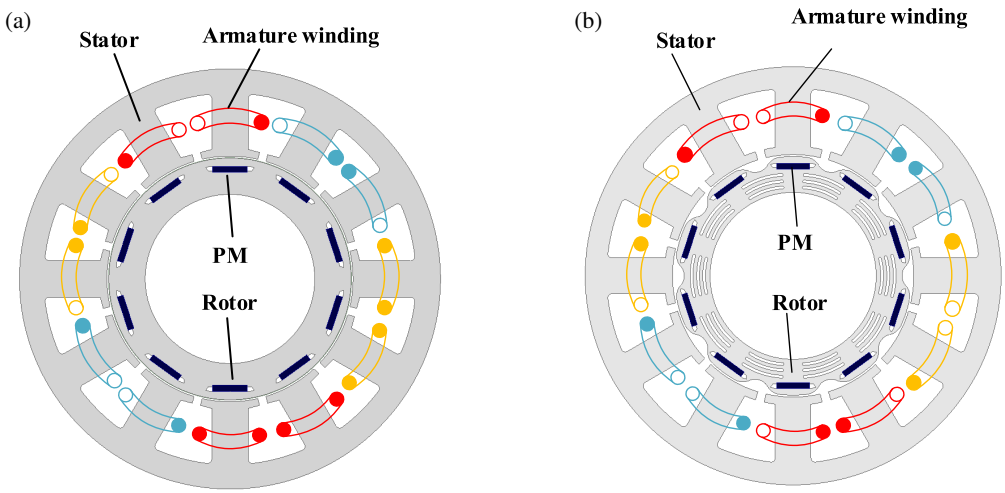

FIGURE 1. Configurations of the two machines. (a) Conventional IPM machine. (b) RS-PMSM.

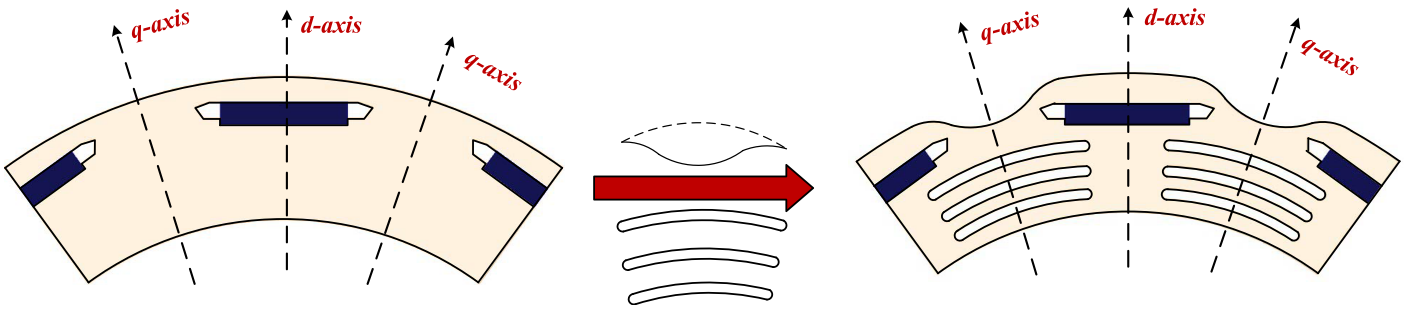

FIGURE 2. Rotor design process.

mances of the machine before and after optimization are compared to verify the effectiveness of the optimized design. In the fourth part, the speed regulation characteristics of RS-PMSM are simulated and analyzed. The speed regulation range and efficiency map plots of RS-PMSM are compared with those of conventional PMSM to demonstrate the wide area and high efficiency characteristics of RS-PMSM.

2. TOPOLOGY AND PRINCIPLES OF MOTOR

2.1. Machine Topology

RS-PMSM, unlike conventional interior PMSM (IPMSM), has a unique rotor structure that allows it to generate an intensifying-flux effect and exhibits reverse-salient characteristics. This design enables RS-PMSM to operate at a broader range of speeds. Fig. 1 illustrates the topologies of both machines. Fig. 1(a) shows the "I" shape interior permanent magnet rotor structure of traditional machine. A 12-slot, 10-pole reverse salient permanent magnet synchronous machine is proposed, with a double-layer fractional-slot non-overlapping centralized winding on the stator side, a interior structure, and a radial-parallel magnetization method of permanent magnet magnetization as shown in Fig. 1(b), where the permanent magnet is embedded in the rotor, and a circular arc flux barrier is constructed in the outer q-axis of the rotor to reduce the inductance of the q-axis. The outer edges of the rotor show a petal-like shape to produce an inhomogeneous air gap, which is gradually increasing from the d-axis to the q-axis.

In conventional PMSM, the internal space of the rotor is constrained, and increasing the number of poles can help indirectly decrease copper loss and torque ripple. However, this necessitates using a larger number of permanent magnets, which presents challenges in terms of rotor lamination stress. In PMSM design, fractional-slot winding possesses several advantages compared to integer-slot winding:

(1) Smaller cogging torque and lower torque ripple;

(2) It can be beneficial for reducing high-order harmonics in the air gap magnetic density and enhancing the waveform of the back electromotive force.

The RS-PMSM rotor structure is gradually evolved from the conventional "I" type IPMSM, and after combining the flux barrier, permanent magnet and other design elements, the final RS-PMSM rotor structure is shown in Fig. 2. Due to the installation of multiple layers of flux barriers within the rotor, the RS-PMSM designed in this study exhibits high torque ripple. Hence, the fractional slot non-overlapping winding design is employed.

2.2. Operating Principle

RS-PMSM reduces the q-axis inductance by placing multiple layers of flux barriers on the q-axis, and in IPMSM, the maxi-

mum speed that can be achieved by RS-PMSM is:

$$n_{\max} = \frac{60U_{\lim}}{2\pi p(\psi_f - L_d I_{\lim})} \tag{1}$$

where $U_{\lim}$ is the limiting voltage, $I_{\lim}$ the limiting current, L_d the d-axis synchronous inductance, ψ_f the flux linkage of PMs, and P the pole pair number. The expansion of the speed range in a machine, particularly during flux-weakening operation, is significantly influenced by two key factors: the flux linkage of PMs and the d-axis inductance. By adjusting these factors, specifically by decreasing the parameter ψ_f and increasing L_d, it is possible to appropriately extend the speed range of the machine. In the case of RS-PMSM operating in high-speed, flux-weakening conditions, a reduction in the q-axis current occurs gradually. This, in turn, leads to a gradual decrease in the leakage of the flux barrier near the flux branch, close to saturation. As a result, the leakage of inter-pole flux from the permanent magnets increases. Ultimately, this process leads to a reduction in the air gap within the permanent magnet flux linkage, leading to an improved speed range for the machine.

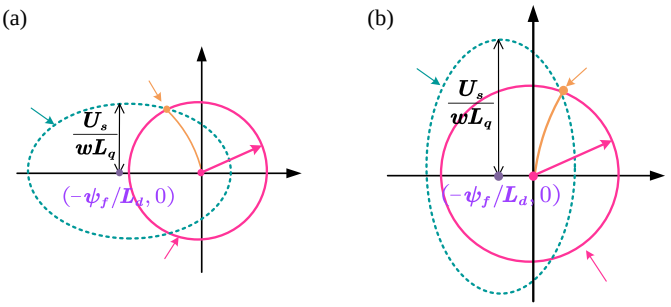

FIGURE 3. Relationship between current and voltage limit circle. (a) Conventional PMSM. (b) RS-PMSM.

This paper delves into RS-PMSM, which incorporates three leakage flux paths to minimize the magnetic reluctance in the leakage paths between permanent magnet poles. When the q-axis current is low in RS-PMSM, it generates more pronounced leakage flux than conventional machines. Consequently, the magnetic flux produced by RS-PMSM is lower than that of conventional machines. The relationship between the current and voltage limit circle of the machines is depicted in Fig. 3. When the Maximum Torque per Ampere (MTPA) control trajectory of a conventional PMSM lies in the second quadrant, the machine operates in a flux-weakening state, indicated by negative d-axis current. In contrast, when the MTPA trajectory of the RS-PMSM is located in the first quadrant, it achieves a flux-intensifying state through positive d-axis current. Clearly, the i_d of the latter exhibits a wider adjustment speed range. As the speed increases, the d-axis current transitions from a flux-intensifying current to a flux-weakening current, which only exists in high-speed conditions. The internal power factor angle adjustment range of RS-PMSM is broader than that of conventional machines. Consequently, RS-PMSM exhibits a wider constant power speed range at low magnetic flux levels.

The permanent magnet synchronous machine electromagnetic torque expression is:

$$T_e = \frac{3}{2} p\left[\psi_f i_q + (L_d - L_q) i_d i_q\right] \tag{2}$$

The electromagnetic torque of a PMSM is composed of two components: the first component is the torque generated by the interaction between the permanent magnet air gap magnetic field and the stator armature reaction magnetic field, known as the permanent magnet torque. The second component is the reluctance torque arising from the asymmetry between the d-axis and q-axis of the machine itself. The total electromagnetic torque of the PMSM results from the combination of the permanent magnet torque and electromagnetic torque. In conventional IPMSM designs, permanent magnets are typically positioned on the d axis to enhance the reluctance in that axis, consequently generating an asymmetry in the q axis and giving rise to reluctance torque. The d axis inductance is usually smaller than the q-axis inductance, i.e., $L_d < L_q$.

Due to its special inductance characteristics, the MTPA current vector trajectory of RS-PMSM is located in the first quadrant, which is beneficial for improving the working point of the permanent magnet. The corresponding working point B_H of the permanent magnet is shown in Fig. 4, at which point the machine exhibits intensifying-flux effect. As the flux-weakening field expands, and the limit voltage circle shrinks, the d-axis current and demagnetization potential of conventional IPMSM in the second quadrant continue to increase, and the risk of irreversible demagnetization also increases. Due to the intensifying-flux effect, the d axis current of RS-PMSM is first positive and then negative. It is also far away from the knee point B_k of the irreversible demagnetization curve of the permanent magnet and has better resistance to the risk of irreversible demagnetization.

3. DESIGN OPTIMIZATION

As a complex system with multiple physical quantities cross-linked, the optimization strategy of machines needs to consider multiple factors comprehensively. The geometric structure, materials, and other factors will affect the performance of the motor to a certain extent. The core of optimization design is to achieve the best performance or lowest cost of the motor under various constraints.

3.1. Machine Optimization Process

This article will adopt a phased optimization strategy to optimize the design of RS-PMSM. Firstly, an RS-PMSM parameterized model was established. Secondly, sensitivity analysis was conducted on each design variable in the parameterized model and stratified, and strong sensitivity design variables were selected for multi-objective optimization. Finally, the NSGA-II algorithm is used for optimization and iterative calculations. The RS-PMSM designed in this paper has intensifying-flux effect, and the basic parameters such as inductance and magnetic link need to be considered in the optimization process. Based on the intensifying-flux effect achieved by RS-PMSM, this section optimizes the target of improving output

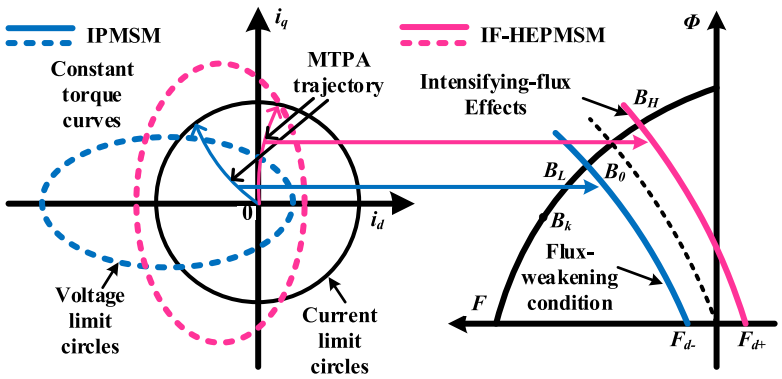

FIGURE 4. Relationship between the limit circle of voltage and current and the working point of PMs.

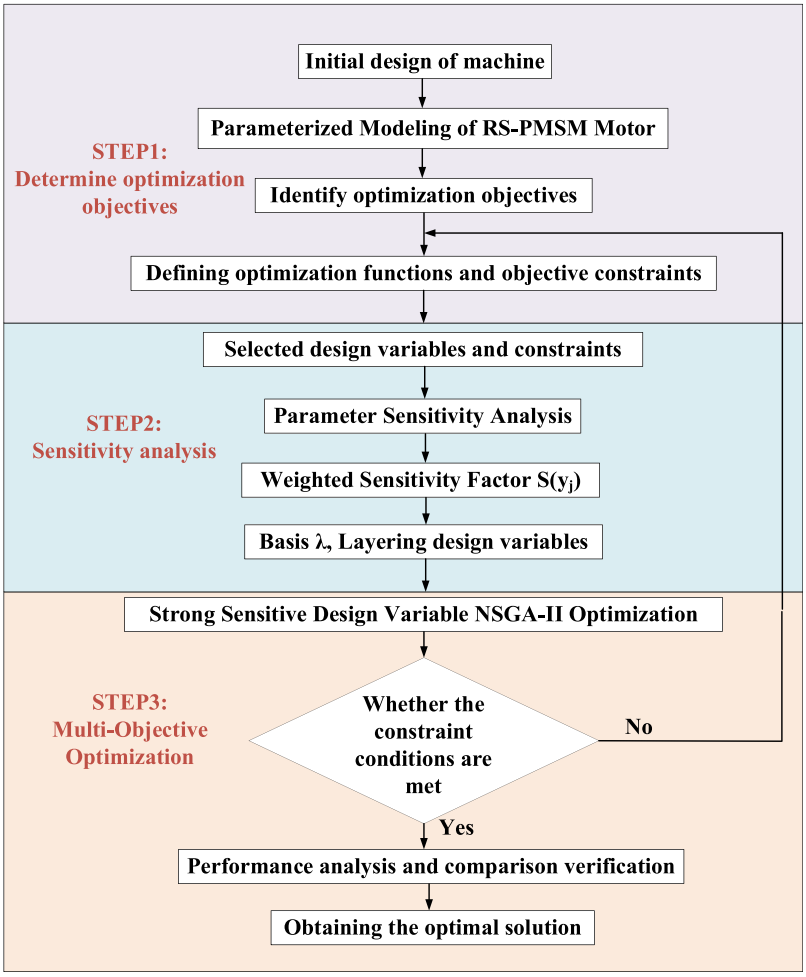

FIGURE 5. Motor optimization flowchart.

torque, reducing torque ripple and increasing reverse salient ratio to obtain the optimal performance topology of RS-PMSM. The phased optimization strategy flowchart is shown in Fig. 5. It mainly includes three steps: determining optimization objectives, sensitivity analysis, and multi-objective optimization.

3.2. Objective Function and Design Variables

The goal of optimization design is to discover the most suitable design solution among many feasible solutions, and this optimization selects three optimization objectives: output torque, torque ripple, and reverse saliency ratio. The output torque T_{out} of RS-PMSM can be expressed as:

$$T_{out} = T_e + T_r \tag{3}$$

where T_e is the electromagnetic torque of the motor, and T_r is the electromagnetic resistance torque of the machine. Torque ripple T_{rip} can be expressed as:

$$T_{rip} = \frac{T_{out\_\max} - T_{out\_\min}}{T_{out}} \times 100\% \tag{4}$$

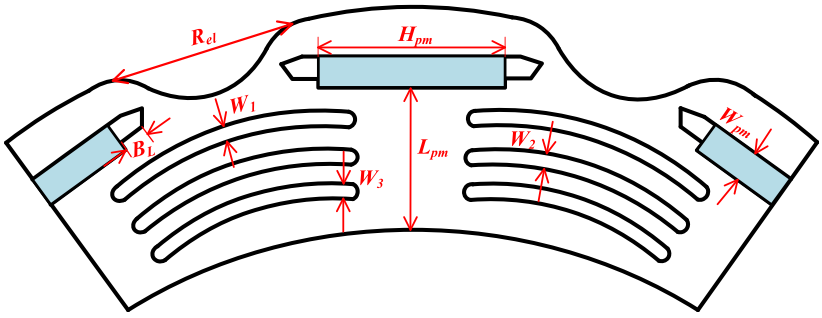

FIGURE 6. RS-PMSM rotor parameterization model.

In the formula, $T_{out\_\max}$ and $T_{out\_\min}$ are the maximum and minimum output torques, respectively. In addition, the inverse convex pole ratio is defined as the ratio of the straight-axis inductance to the cross-axis inductance k:

$$k = \frac{L_d}{L_q} \tag{5}$$

The weighted objective function for the entire optimization process is:

$$f(y_j)_{\min} = \xi_1 \frac{T^*_{out}(y_j)}{T_{out}(y_j)} + \xi_2 \frac{T^*_{rip}(y_j)}{T_{rip}(y_j)} + \xi_3 \frac{k^*(y_j)}{k(y_j)}$$

$$\min\, y_j \leqslant y_j \leqslant \max\, y_j,\ \ j = 1, 2, 3, 4 \tag{6}$$

where $T^*_{out}(y_j)$, $T^*_{rip}(y_j)$, $k^*(y_j)$ are initial values of output torque, torque ripple, and reverse saliency ratio, respectively. $T_{out}(y_j)$, $T_{rip}(y_j)$, $k(y_j)$ are optimal values of output torque, torque ripple, and reverse saliency ratio, respectively. The boundary constraint of RS-PMSM is:

$$T_{out} \geqslant 15N;\ \ T_{rip} \leqslant 15\%;\ \ k \geqslant 1 \tag{7}$$

In addition, the variation range of RS-PMSM rotor design variables and parameters is listed in Table 1. For illustration purposes, the parameterized model of RS-PMSM rotor structure is given in Fig. 6.

TABLE 1. Design variables and variation ranges.

Design Variables	Variation Ranges
L_{pm}	[37 mm, 41 mm]
W_{pm}	[1.8 mm, 2.5 mm]
H_{pm}	[12 mm, 15 mm]
R_{el}	[1 mm, 3.5 mm]
W_1	[1 mm, 2.5 mm]
W_2	[1 mm, 2.5 mm]
W_3	[1 mm, 2.5 mm]
B_L	[1 mm, 2.4 mm]

3.3. Sensitivity Analysis

Sensitivity analysis results can characterize the degree between design variables and optimization objectives. Coefficients of prognosis (Cop) are introduced as correlation analysis indicators. The size of the values can reflect the correlation between design variables and optimization objectives to determine whether the design is suitable for optimization. In this paper, the prediction coefficient expression is:

$$CoP(y_j) = \left(1 - \frac{SS^P_E}{SS_T}\right) \cdot S^{MOP}_T(y_j) \tag{8}$$

$$S^{MOP}_T(y_j) = 1 - \frac{V\left(f(y_j)|y_{\sim j}\right)}{V\left(f(y_j)\right)} \tag{9}$$

where SS_T and SS^P_E are respectively the total variation and unexplained variation; $S^{MOP}_T(y_j)$ is the total effect sensitive factor; and $V(f(y_j))$ is the variance of $f(y_j)$ generated by variables other than y_j. According to Equation (9), define the calculation method and perform Cop calculation. Fig. 7 shows the results of the prediction coefficient calculation matrix.

In sensitivity analysis, there are different correlations between design variables and optimization objectives, and the degree of their impact can be characterized by predictive coefficients. The predicted coefficient value between the distance of the permanent magnet from the inner diameter of the rotor L_{pm} and the output torque T_{out} is 31.4%, reflecting the highest degree of influence of the permanent magnet flux bridge on the torque output ability among various design variables. The reverse saliency ratio is mainly determined by the length of the permanent magnet R_{el}, H_{pm}, and the predicted coefficient value between it and torque ripple T_{rip} is 26.4% and 31.8%. Torque ripple can be suppressed by changing the length of the permanent magnet. The disadvantage is that univariate analysis is difficult to determine the optimal value of design variables, and further trade-offs are needed.

3.4. Design Variable Stratification

To select key design variables for multi-objective optimization, a comprehensive trade-off index is introduced that characterizes the comprehensive impact of design variables, defined as:

$$S(y_j) = \xi_1 \cdot Cop_{out}(y_j) + \xi_2 \cdot Cop_{rip}(y_j) + \xi_3 \cdot Cop_k(y_j) \tag{10}$$

where y_j is the design variable for multi-objective optimization, and $Cop_{out}(y_j)$, $Cop_{rip}(y_j)$, $Cop_k(y_j)$ are the coefficients of prognosis of the selected design variable for output torque, torque ripple, and reverse saliency ratio. According to the prediction coefficient matrix in Fig. 7 and Equations (3)–(5), the

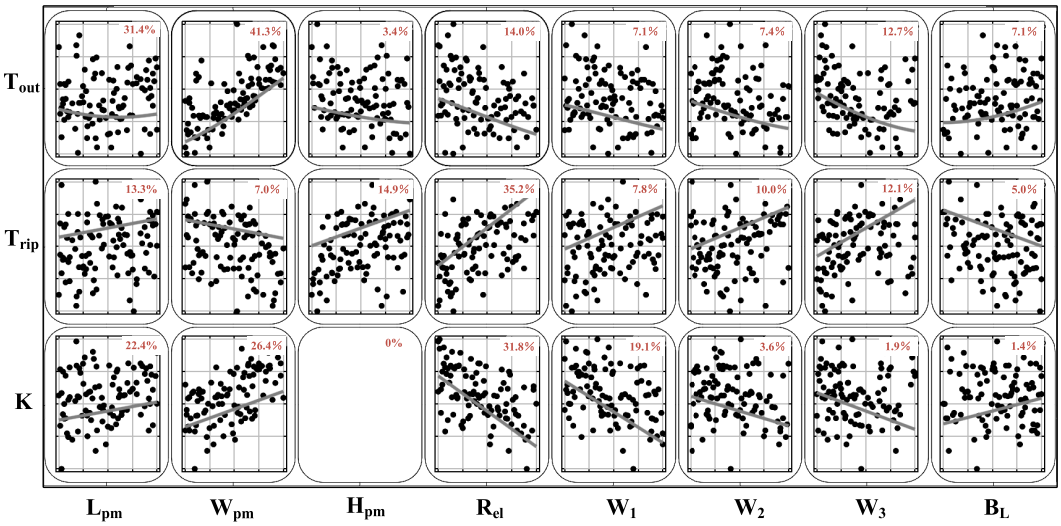

FIGURE 7. Cop matrix.

TABLE 2. Cop of prognosis and comprehensive trand-off index.

design variable	prediction coefficient (%)			Comprehensive balance index
	$Cop_{out}(y_j)$	$Cop_{rip}(y_j)$	$Cop_k(y_j)$	$S(y_j)(\%)$
L_{pm}	31.4	13.3	22.4	22.4
W_{pm}	41.3	7.0	26.4	24.9
H_{pm}	3.4	14.9	0	6.1
R_{el}	14.0	35.2	31.8	27
W_1	7.1	7.8	19.1	11.3
W_2	7.4	10.0	3.6	7
W_3	12.7	12.1	1.9	8.9
B_L	7.1	5.0	1.4	4.5

comprehensive trade-off index can be calculated. The calculation results are shown in Table 2.

According to the comprehensive balance index in Table 3, the design variables are stratified and divided into strongly sensitive and insensitive design variables. Among them, strongly sensitive design variables have a significant impact on the optimization objectives and will be included in further multiobjective optimization processes, while insensitive design variables will continue to use their initial values. The hierarchical results of design variables are shown in Table 3, where W_{pm}, H_{pm}, R_{el} are selected as sensitive design variables, and W_1, W_2, W_3, L_{pm}, B_L are selected as insensitive design variables.

TABLE 3. Stratification of the design variables.

Classification	Selected parameters
Sensitive	W_{pm}, L_{pm}, R_{el}
Insensitive	W_1, W_2, W_3, B_L, H_{pm}

3.5. Multiobjective Optimization Results

NSGA-II has fast operation speed and good convergence, making it suitable for motor optimization design. Based on the hierarchical results of design variables, strong sensitive design variables are selected to establish a sample space, and the NSGA-II algorithm is used to form Pareto front surfaces for three optimization objectives, as shown in Fig. 8. The optimal solution for the least optimization is obtained and annotated in the figure.

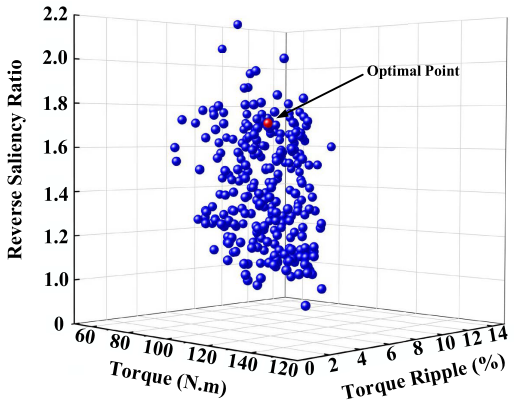

FIGURE 8. Pareto front surfaces.

The comparison of sensitive design variables before and after optimization is shown in Table 4, and the optimization objectives are listed for comparison. The insensitive design vari-

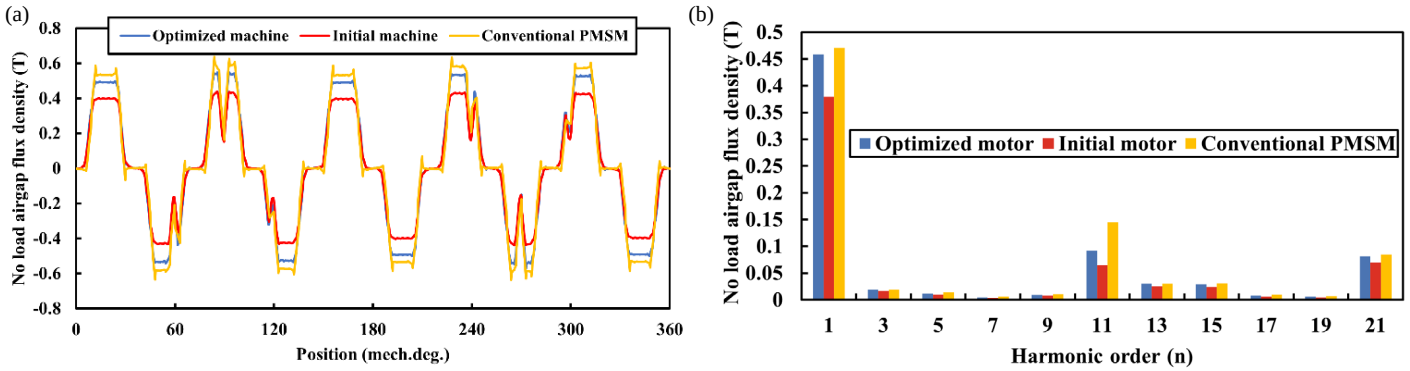

FIGURE 9. Air-gap flux density of optimized machine, initial machine and conventional PMSM. (a) Waveforms. (b) Harmonics.

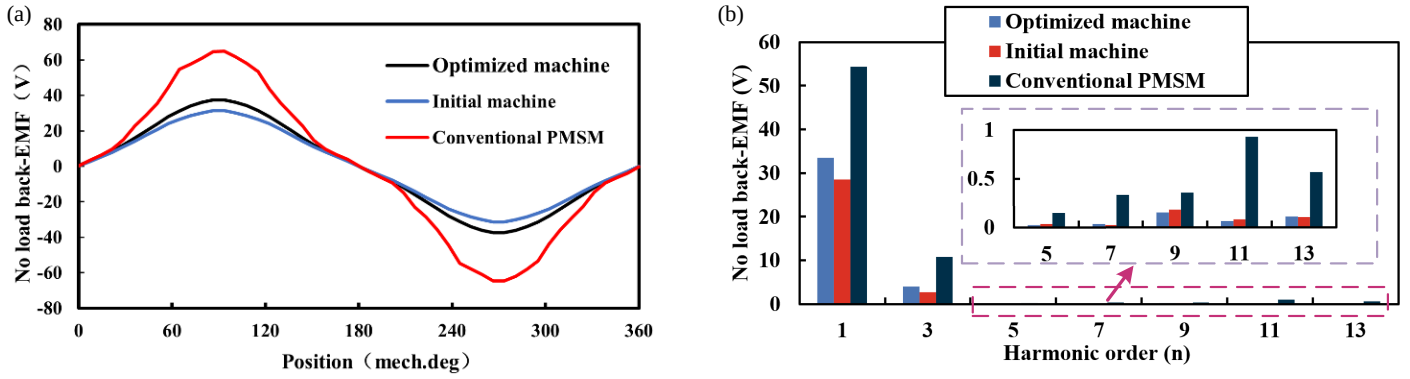

FIGURE 10. No-load back-EMF waveform of optimized machine, initial machine and conventional PMSM. (a) Waveforms. (b) Harmonics.

ables remain unchanged at their initial design values. From the data in Table 4, it can be seen that the sensitive design variables have been adjusted accordingly after multi-objective optimization. Among them, the output torque increased from 21.4 N·m to 23.4 N·m, with an optimization amplitude of 9.3%, and the torque ripple decreased from 9.5% to 8.7%, with an optimization amplitude of 8%. The reverse saliency ratio has been increased from 1.03 to 1.10, with an optimization margin of 6.7%. In summary, it can be seen that the optimal solution selected after multi-objective optimization meets the objective function and constraint conditions, obtaining the optimal performance topology of RS-PMSM and verifying the effectiveness of phased optimization strategy and optimization design.

TABLE 4. Comparison of main parameters before and after optimization.

Design variables	Initial values	Optimal values
L_{pm}	38.5 mm	40.5 mm
R_{el}	2.5 mm	3.2 mm
W_{pm}	3.2 mm	2.0 mm
T_{out}	17.8 N·m	19.6 N·m
T_{rip}	9.5%	3.3%
k	1.03	1.20

4. ELECTROMAGNETIC ANALYSIS

This section employs finite element simulation analysis to scrutinize and assess the optimal performance topology of the RS-PMSM, which has been achieved through multi-objective optimization. It also entails the computation of air-gap flux density, back-electromotive force, torque characteristics, and inductance characteristics.

4.1. No-Load Characteristics

To confirm the reliability of the RS-PMSM structural design, it is essential to examine its no-load characteristics.

The air gap flux density reflects the machine's output torque capability and will have an impact on torque performance and noise and vibration. Fig. 11 gives the results of the air-gap flux density waveforms and the associated harmonic content analysis before and after the RS-PMSM optimization with the conventional machine. From Fig. 9(a), the RS-PMSM initial motor air-gap flux density amplitude is 0.44 T, and the optimized machine air-gap flux density amplitude is 0.55 T. The optimized air-gap flux density amplitude is improved. However, the RS-PMSM air-gap flux density is lower than the conventional motor air-gap flux density, which is due to the limited space inside the rotor and the existence of leakage loops that lead to low utilization of permanent magnets, so the fundamental amplitude of the RS-PMSM is slightly smaller than that of the conventional motor, as shown in Fig. 9(b). The 3rd harmonic and 5th

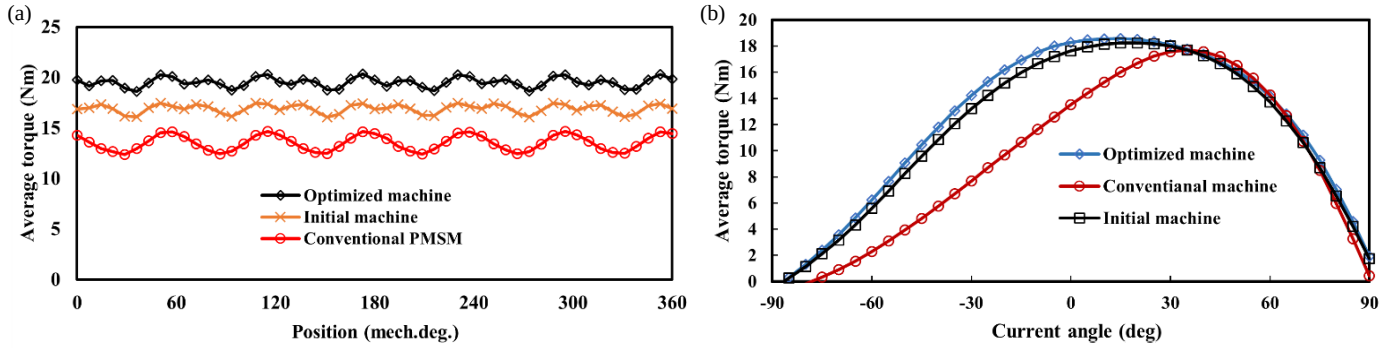

FIGURE 11. Output torque characteristics. (a) Output torque at rated operation condition ($J = 5\,\mathrm{A/mm^2}$). (b) Average torque versus current angle curve.

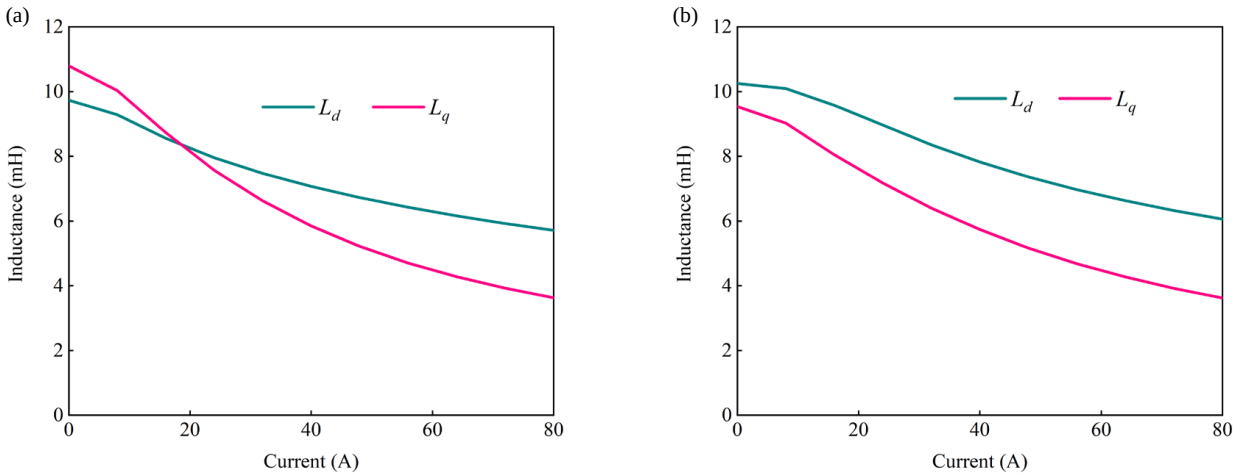

FIGURE 12. Inductance characteristics. (a) Initial motor. (b) Optimized motor.

harmonic of the RS-PMSM are smaller than that of the conventional machine, which means that its torque ripple is smaller.

The no-load back electromotive force waveforms and the associated harmonic content analysis of the RS-PMSM before and after optimization versus the conventional motor are given in Fig. 10. The optimized back electromotive force (EMF) amplitude of the RS-PMSM is 37.4 V, which represents a 19.4% increase compared to the initial machine. The optimized RS-PMSM exhibits the highest concentration of high harmonics in the 3rd harmonic, with other high harmonics being relatively low. Comparatively, the Total Harmonic Distortion (THD) for the RS-PMSM is 3.2%, while conventional motors have a higher THD of 8.7%. This reduced THD in the RS-PMSM can be attributed to the smaller amplitudes of the 3rd, 5th, 9th, and 11th harmonics in contrast to conventional machines. Additionally, the back EMF waveform of the optimized RS-PMSM closely approximates a sinusoidal waveform, in contrast to the conventional machine. This observation suggests that the design of the rotor structure for the RS-PMSM is more optimal, leading to enhanced precision in machine control.

4.2. Torque Characteristic

Figure 11(a) presents the average torque output curves of the RS-PMSM before and after optimization, in comparison with a conventional machine, under rated operating condition ($J = 5\,\mathrm{A/mm^2}$). The output torque is 17.4 N·m before optimization and 19.7 N·m after optimization, which is a 13.2% increase in output torque. Compared with the conventional machine, the output torque increases by 16.7%, and the torque ripple decreases by 5.1%, which improves the stability of the machine operation. In order to objectively evaluate the torque output capability of RS-PMSM, the curve of current angle versus average torque change is shown in Fig. 11(b). The conventional machine achieves the maximum average torque of 17.2 N·m at the current angle of 35 deg, and the d-axis current is -29.4 A, whereas the optimized RS-PMSM achieves the maximum average torque at the current angle of 10 deg, and the d-axis current is -8 A, which implies that the conventional machine's demagnetization risk is higher than RS-PMSM. However, the optimized RS-PMSM does not achieve the maximum average torque at negative angle of current angle, because of the large weighting coefficient of the output torque as the optimization objective in the optimization process. If the reverse salient pole ratio is the main optimization objective, a large output torque is sacrificed to achieve positive reluctance torque.

4.3. Inductance Characteristic

The flux-weakening capability and speed range of the RS-PMSM are closely tied to its inductance characteristics. Fig. 12 illustrates the variation of the dq-axis inductance with current

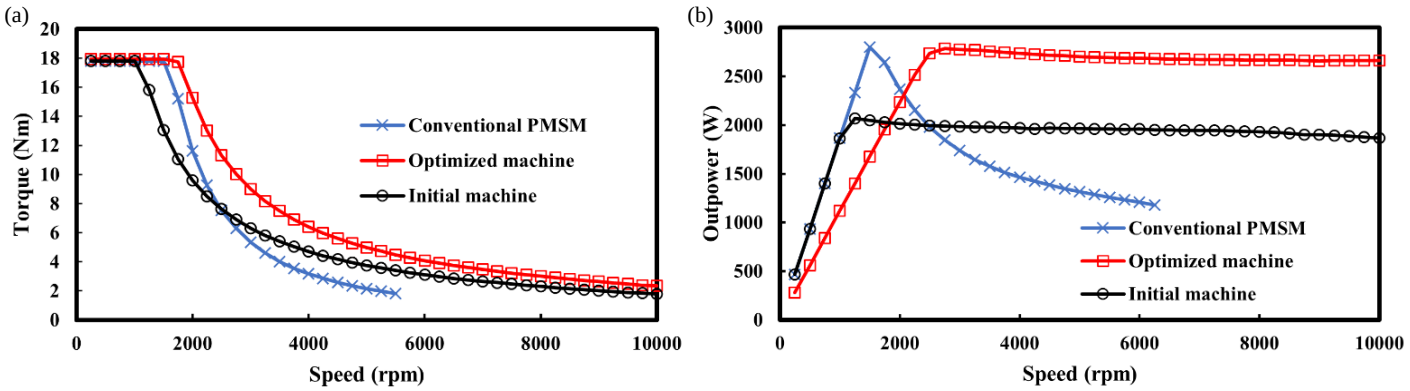

FIGURE 13. (a) Torque-speed curves of the two machines. (b) Power-speed curves of the two machines.

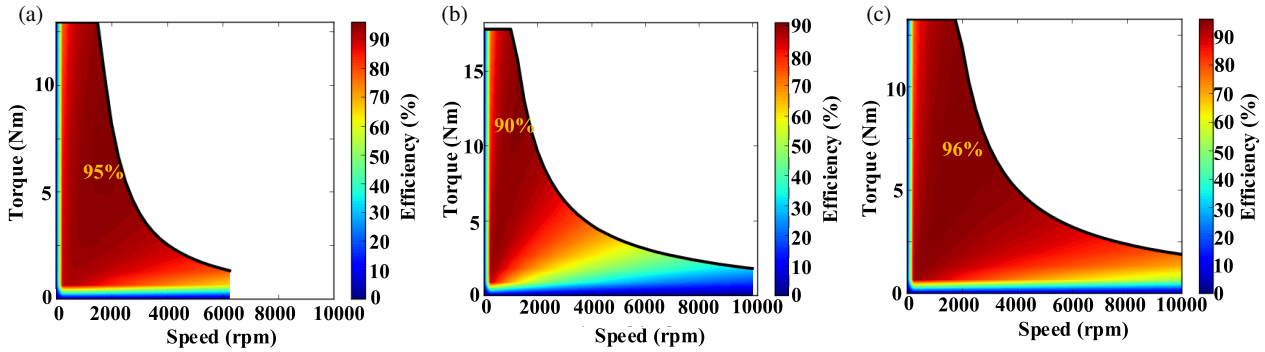

FIGURE 14. Efficiency map of machines. (a) Conventional machine. (b) Initial machine. (c) Optimized machine.

both before and after the optimization of the RS-PMSM. In the optimized RS-PMSM, L_d consistently surpasses L_q throughout the entire current range. This is primarily attributed to the larger cross-axis magnetic barrier in the optimized design, which significantly reduces the q-axis inductance. As the current increases from 0 A to 80 A, there is a notable decline in dq-axis inductance. This decline can be attributed to the deepening saturation of the rotor-side leakage region, leading to an increase in dq-axis magnetoresistance and, consequently, a reduction in dq-axis inductance.

4.4. Analysis of Speed Regulation Characteristics

PMSM employs a specialized current control technique known as flux-weakening control to enable the machine to operate above its rated speed while adhering to the voltage and current limits of the inverter. This control strategy is instrumental in extending the range of machine speed regulation. In the context of this research, the designed machine is intended for the use in electric vehicles, where a broad speed range is a crucial design criterion. To demonstrate the robust flux-weakening capabilities and wide speed range of the RS-PMSM, a conventional IPMSM with the same rated power serves as a basis for comparison.

Through finite element simulation, torque-speed and power-speed curves for both machines were generated, as illustrated in Fig. 13(a). Analysis of these curves reveals that when running at or below rated speed, both machines provide a consistent output torque of approximately 17.8 N·m. However, as the speed exceeds the rated value, they enter a flux-weakening region where the output torque decreases proportionally with the degree of flux-weakening. Notably, the conventional IPMSM reaches a maximum speed of 5500 rpm, whereas the RS-PMSM achieves speeds exceeding 10000 rpm. Consequently, the RS-PMSM exhibits the widest speed range, with a speed regulation ratio exceeding $1:6$. In Fig. 13(b), the power-speed curve is presented. Below the rated speed, the output powers for both machines increase with rising speed. At the rated speed, the output power matches the machine's rated power. However, as the speed continues to increase, the output powers of the two machines behave differently. The conventional IPMSM experiences a sharp decline in output power as the speed increases, while the RS-PMSM maintains a relatively constant output power. This highlights the fact that the RS-PMSM offers a broader range of constant power speed regulation. In summary, the RS-PMSM, designed for electric vehicle applications, excels in terms of flux-weakening capability and an extended speed range, making it a valuable choice for scenarios demanding high-speed performance and constant power output.

4.5. Analysis of RS-PMSM Efficiency

The efficiency map in Fig. 14 illustrates the performance of RS-PMSM before and after optimization, as well as a comparison with conventional motors. All three motors exhibit their highest efficiency near their rated speeds. The initial RS-PMSM

TABLE 5. Comparison results of the three investigated machines.

Model	Conventional machine [7]	Initial machine	Optimized machine
Average torque (N·m)	14.8	17.4	19.7
Torque ripple (%)	15.1	9.5	3.3
Air-gap density (T)	0.65	0.44	0.55
No load back-EMF (V)	65.3	35.2	37.4
L_d/L_q	0.88	1.03	1.2
Efficiency (%)	95%	90%	96%
Base Speed (r/min)	1500	1250	1500
Max. Speed (r/min)	5800	10000	10000

achieves a maximum efficiency of 90%, whereas the optimized RS-PMSM reaches an impressive maximum efficiency of 96%. For speeds up to 6000 rpm, the optimized RS-PMSM consistently maintains an efficiency of approximately 85%. In contrast, a conventional motor can sustain an efficiency about 70% at its maximum speed of 6,250 rpm. What's noteworthy is that the optimized RS-PMSM continues to operate efficiently at over 70% even in the high-speed range of 8,000 rpm. This represents a significant advantage, with a speed range 1.6 times that of a conventional motor. In conclusion, the optimization of the RS-PMSM has resulted in a motor with a superior efficiency distribution compared to both its initial version and conventional machine. The machine's ability to achieve higher efficiencies at various speed ranges, especially in the high-speed region, makes it an attractive choice for various applications where efficiency and performance are critical.

Additionally, the comparison results of the three machines are examined. Firstly, the average torque, torque ripple, no-load air-gap density, no-load back-EMF, d/q-axis inductance, efficiency, and base/maximum speed are presented in Table 5. It is evident that the proposed RS-PMSM demonstrates superior flux-weakening capability, primarily due to the largest reverse salient ratio (L_d/L_q). This results in a significantly expanded speed range for the proposed machine.

5. CONCLUSION

A novel reverse-salient PMSM with the characteristics of $L_d > L_q$ is proposed in this paper. The working principle of RS-PMSM is clarified; the detailed design of the motor rotor is carried out; the multi-objective optimization of the initial design scheme of RS-PMSM is carried out; and the motor performances before and after optimization are compared and analyzed to verify the rationality and effectiveness of the stage-wise optimization strategy and the optimized motor design. Then, the speed regulation characteristics and efficiency of RS-PMSM and conventional PMSM are compared and analyzed to verify the characteristics of RS-PMSM wide area and high efficiency. The following conclusions are drawn.

(a) A novel intensifying-flux rotor structure is proposed with the characteristic of $L_d > L_q$. L_d is 1.08 times higher than L_q.

(b) Multi-objective optimization using NSGA-II is performed, and the simulation results demonstrate that the optimized design of the RS-PMSM has improved no-load characteristics, 10.5% improvement in no-load counter-electromotive force, and output torque increased by 17.1%.

(c) The proposed RS-PMSM exhibits an improved flux weakening capability with a variable flux-leakage, resulting in a wider operational speed range, speed regulation ranges up to $6.6:1$.

REFERENCES

[1] Amara, Y., S. Hlioui, H. B. Ahmed, and M. Gabsi, "Power capability of hybrid excited synchronous motors in variable speed drives applications," *IEEE Transactions on Magnetics*, Vol. 55, No. 8, 1–12, Aug. 2019.

[2] Ai, Q., H. Wei, T. Li, L. Fan, and Y. Zhang, "Optimisation of reverse salient rotor for interior permanent magnet synchronous motor and experimental validation," *IET Electric Power Applications*, Vol. 15, No. 12, 1547–1563, 2021.

[3] Bianchi, N. and S. Bolognani, "Performance analysis of an IPM motor with segmented rotor for flux-weakening applications," in *Ninth International Conference on Electrical Machines and Drives (Conf. Publ. No. 468)*, 49–53, Canterbury, Sep. 1999.

[4] Dianov, A., F. Tinazzi, S. Calligaro, and S. Bolognani, "Review and classification of MTPA control algorithms for synchronous motors," *IEEE Transactions on Power Electronics*, Vol. 37, No. 4, 3990–4007, Apr. 2022.

[5] Huang, W., B. Du, T. Li, Y. Sun, Y. Cheng, and S. Cui, "Interturn short-circuit fault diagnosis of interior permanent magnet synchronous motor for electric vehicle based on search coil," *IEEE Transactions on Power Electronics*, Vol. 38, No. 2, 2506–2515, Feb. 2023.

[6] Liu, W., H. Yang, H. Lin, and X. Liu, "Influence of low-coercive-force magnet property on electromagnetic performance of variable flux memory machine," *IEEE Transactions on Magnetics*, Vol. 58, No. 8, 1–6, Aug. 2022.

[7] Liu, F., L. Quan, X. Zhu, L. Ge, and W. Wu, "Reverse saliency optimization of flux-intensifying hybrid permanent magnet machine for variable speed applications," *IEEE Transactions on Applied Superconductivity*, Vol. 29, No. 2, 1–5, Mar. 2019.

[8] Liu, X., Y. Li, Z. Liu, T. Ling, and Z. Luo, "Analysis and design of a high power density permanent magnet-assisted synchronous reluctance machine with low-cost ferrite magnets for EVs/HEVs," *COMPEL — The International Journal for Computation and Mathematics in Electrical and Electronic Engineering*, Vol. 35, No. 6, 1949–1964, 2016.

[9] Limsuwan, N., T. Fukushige, K. Akatsu, and R. D. Lorenz, "Design methodology for variable-flux, flux-intensifying interior permanent magnet machines for an electric-vehicle-class in-

verter rating," in *2013 IEEE Energy Conversion Congress and Exposition*, 1547–1554, Denver, CO, USA, Sep. 2013.

[10] Moncada, R. H., J. A. Tapia, and T. M. Jahns, "Inverse-saliency PM motor performance under vector control operation," in *2009 IEEE Energy Conversion Congress and Exposition*, 2368–2373, San Jose, CA, USA, 2009.

[11] Michieletto, D., L. Cinti, and N. Bianchi, "Hybrid excitation PM synchronous motors: Part I — Per unit analysis," *IEEE Transactions on Energy Conversion*, Vol. 37, No. 1, 487–494, 2022.

[12] Mohammadi, A. S., J. P. F. Trovão, and C. H. Antunes, "Component-level optimization of hybrid excitation synchronous machines for a specified hybridization ratio using NSGA-II," *IEEE Transactions on Energy Conversion*, Vol. 35, No. 3, 1596–1605, 2020.

[13] Ngo, D.-K., M.-F. Hsieh, and T. A. Huynh, "Torque enhancement for a novel flux intensifying PMA-SynRM using surface-inset permanent magnet," *IEEE Transactions on Magnetics*, Vol. 55, No. 7, 1–8, 2019.

[14] Villani, M., M. Tursini, G. Fabri, and L. Castellini, "High reliability permanent magnet brushless motor drive for aircraft application," *IEEE Transactions on Industrial Electronics*, Vol. 59, No. 5, 2073–2081, 2012.

[15] Kim, W.-H., K.-S. Kim, S.-J. Kim, D.-W. Kang, S.-C. Go, Y.-D. Chun, and J. Lee, "Optimal PM design of PMA-SynRM for wide constant-power operation and torque ripple reduction," *IEEE Transactions on Magnetics*, Vol. 45, No. 10, 4660–4663, 2009.

[16] Xiao, Y., Z. Q. Zhu, G. W. Jewell, J. T. Chen, D. Wu, and L. M. Gong, "A novel asymmetric interior permanent magnet synchronous machine," *IEEE Transactions on Industry Applications*, Vol. 58, No. 3, 3370–3382, 2022.

[17] Xu, H., J. Li, J. Chen, Y. Lu, and M. Ge, "Analysis of a hybrid permanent magnet variable-flux machine for electric vehicle tractions considering magnetizing and demagnetizing current," *IEEE Transactions on Industry Applications*, Vol. 57, No. 6, 5983–5992, 2021.

[18] Zhu, X., W. Wu, S. Yang, Z. Xiang, and L. Quan, "Comparative design and analysis of new type of flux-intensifying interior permanent magnet motors with different Q-axis rotor flux barriers," *IEEE Transactions on Energy Conversion*, Vol. 33, No. 4, 2260–2269, 2018.

[19] Zhu, X., S. Yang, Y. Du, Z. Xiang, and L. Xu, "Electromagnetic performance analysis and verification of a new flux-intensifying permanent magnet brushless motor with two-layer segmented permanent magnets," *IEEE Transactions on Magnetics*, Vol. 52, No. 7, 1–4, 2016.

[20] Zhao, X., B. Kou, C. Huang, and L. Zhang, "A reverse-salient permanent magnet synchronous motor for electric vehicles considering operating conditions," *IEEE Transactions on Energy Conversion*, Vol. 38, No. 1, 262–272, 2023.

[21] Zhu, X., J. Huang, L. Quan, Z. Xiang, and B. Shi, "Comprehensive sensitivity analysis and multiobjective optimization research of permanent magnet flux-intensifying motors," *IEEE Transactions on Industrial Electronics*, Vol. 66, No. 4, 2613–2627, 2019.